

Purity-dependent Lorenz number, electron hydrodynamics and electron-phonon coupling in WTe₂

Wei Xie¹, Feng Yang¹, Liangcai Xu¹, Xiaokang Li¹, Zengwei Zhu^{1,*} and Kamran Behnia^{2,*}

¹Wuhan National High Magnetic Field Center and School of Physics,
Huazhong University of Science and Technology, Wuhan, 430074, China

²Laboratoire de Physique et Etude des Matériaux (CNRS/UPMC),
Ecole Supérieure de Physique et de Chimie Industrielles, 10 Rue Vauquelin, 75005 Paris, France

(Dated: December 29, 2023)

We present a study of electrical and thermal transport in Weyl semimetal WTe₂ down to 0.3 K. The Wiedemann–Franz law holds below 2 K and a downward deviation starts above. The deviation is more pronounced in cleaner samples, as expected in the hydrodynamic picture of electronic transport, where a fraction of electron-electron collisions conserve momentum. Phonons are the dominant heat carriers and their mean-free-path do not display a Knudsen minimum. This is presumably a consequence of weak anharmonicity, as indicated by the temperature dependence of the specific heat. Frequent momentum exchange between phonons and electrons leads to quantum oscillations of the phononic thermal conductivity. Bloch–Grüneisen picture of electron-phonon scattering breaks down at low temperature when Umklapp ph-ph collisions cease to be a sink for electronic flow of momentum. Comparison with semi-metallic Sb shows that normal ph-ph collisions are amplified by anharmonicity. In both semimetals, at cryogenic temperature, e-ph collisions degrade the phononic flow of energy but not the electronic flow of momentum.

Semi-metallic WTe₂ attracted much attention, first because of its large magnetoresistance [1–3], and then following its identification as a type-II Weyl semimetal [4]. It has a carrier density as low as $n = p \simeq 6.8 \times 10^{19} \text{ cm}^{-3}$ [2]. This implies that several hundred primitive cells share a single mobile electron (as well as a mobile hole). Its large orbital magnetoresistance is due to the high mobility of carriers whose long wavelength attenuates scattering by point-like defects. Thanks to compensation, magnetoresistance does not saturate in the high-field limit. Such features are also detectable in other semi-metals such as antimony ($n = p = 5.5 \times 10^{19} \text{ cm}^{-3}$) [5, 6] and in WP₂ ($n = p = 1.5 \times 10^{21} \text{ cm}^{-3}$) [7, 8].

Recently, thermal transport in both WP₂ [7, 8] and in Sb [5, 9] has been studied in order to detect signatures of hydrodynamics. These are expected when a significant portion of collisions between particles conserve momentum instead of relaxing it. This idea was first put forward, decades ago by Gurzhi [10], who proposed the possibility of viscous flow of electrons in metals and phonons in insulators. A renewal of interest in this topic has led to the experimental scrutiny of thermal transport by electrons [5, 7, 11] and by phonons [9, 12–14], as well as a number of theoretical studies [15–18].

Here, we present a study of electrical, σ , and thermal, κ , conductivities in bulk WTe₂ single crystals with different residual resistivities from 100 K down to 0.3 K. We quantify the Lorenz ratio $L = \frac{\kappa}{T\sigma}$ and find that it exceeds the Sommerfeld value of $L_0 = \frac{\pi^2}{3} \frac{k_B^2}{e^2}$. This means that, in our range of investigation, thermal conductivity by phonons dominates heat transport. Using a magnetic field, we can separate the electronic (κ_e) and the phononic (κ_{ph}) components of the thermal conductivity. We find that $\frac{\kappa_e}{T\sigma} \simeq L_0$ at 2 K, thus, the Wiedemann–Franz (WF) law holds in the zero temperature limit, when inelastic scattering is absent. As the tem-

perature increases, $\frac{\kappa_e}{T\sigma}$ begins to fall below L_0 . Thermal resistivity, defined as $(\kappa/T)^{-1}$ follows T^2 with a prefactor larger than that of the T^2 prefactor of electrical resistivity, as previously reported in other metals [5, 8, 19–22]. By comparing samples with different residual resistivities, we find that the deviation from the WF law increases with the increase of the mean-free-path, as expected in the hydrodynamic picture of heat transport [15].

The phononic thermal conductivity, κ_{ph} , of WTe₂, displays quantum oscillations, indicating significant electron-phonon coupling, providing an explanation for the absence of ballistic phonon transport down to 0.3 K. In contrast to antimony [5, 9], there is no local Knudsen minimum in the temperature dependence of phonon mean-free-path, indicating the absence of phonon hydrodynamics. and in contrast to antimony, the phonon specific heat displays an asymptotic Debye T^3 temperature dependence, indicating weak normal ph-ph scattering in WTe₂. Nevertheless, like in antimony, below a threshold temperature, the Bloch–Grüneisen picture of electron-phonon resistivity is suddenly interrupted. Below this temperature, the electronic flow do not lose momentum because of e-ph collisions.

As shown in figure 1a, we used a standard one-heater-two-thermometers method to measure thermal conductivity (for details see the supplement). Electrical and heat currents were applied along the a axis and the magnetic field was oriented perpendicular to them. Figure 1b presents the temperature dependence of electrical resistivity in three different WTe₂ samples with RRR ratio ($\rho(300 \text{ K})/\rho(2 \text{ K})$) of 250, 540 and 840 respectively. The carrier mean-free-path ℓ_0 , estimated by the Drude formula is in the range of 3.2–13.2 μm , smaller than the size of our samples. The inset shows the same data as a function of T^2 . One can see that resistivity varies quadratically with temperature. The temperature dependence of

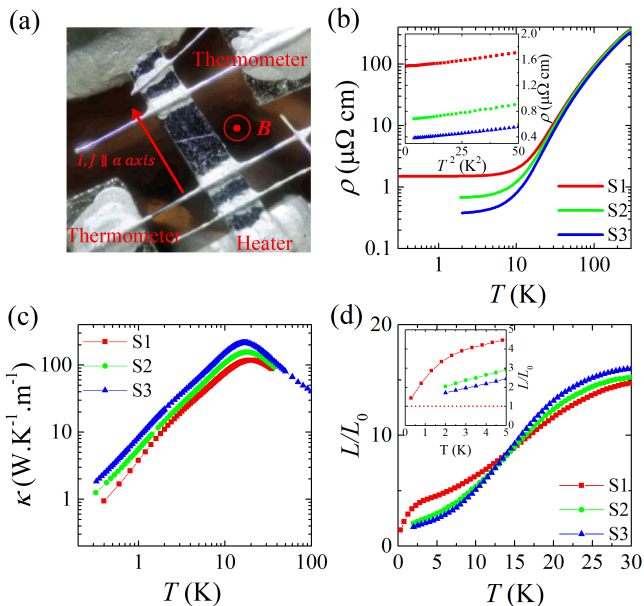


FIG. 1. **Electrical and thermal transport in absence of magnetic field.** (a) A photograph of the sample, the contacts for measuring local temperature and electric field and the thermometers. (b) Temperature dependence of the electrical resistivity of three WTe_2 samples. The insert shows the low temperature data as a function of T^2 . (c) Temperature dependence of the thermal conductivity of three WTe_2 samples. (d) The L/L_0 ratio as a function of temperature. The insert is a zoom on the low temperature data displaying the recovery of the WF law in the zero temperature limit.

thermal conductivity (κ) of the same samples are shown in figure 1c. κ peaks in all three around 18 K. Below this maximum, κ quickly decreases. The temperature dependence of L/L_0 is presented in figure 1d. Here L is the experimentally measured Lorenz number and L_0 is the Sommerfeld value set by fundamental constants. Within our temperature range of measurements, $L/L_0 > 1$, but when the temperature is close to zero, it tends towards unity in conformity with the WF law.

The scrutiny of the L/L_0 is instructive. In WP_2 , another Weyl semi-metal, L/L_0 becomes less than unity at cryogenic temperatures [7, 8], and tends towards in the zero-temperature limit [8]. This means that the phononic contribution to the thermal transport is negligible in WP_2 , which has ≈ 20 times more carriers than WTe_2 . On the other hand, in graphite [14] (which has 20 times less carriers) and in Sb [9] (which has almost the same carrier density), the L/L_0 ratio exceeds unity when the sample is warmed. These are the cases where the phononic component of thermal conductivity accounts for a significant part of the total thermal conductivity. In addition to the phonon contribution, ambipolar contribution can also enhance the Lorenz ratio [23], but only when carriers are warmed above their degeneracy temperature, which is not the case here.

In order to separate phononic and electronic compo-

nents of the total thermal conductivity, we can exploit magnetic field and the fact that it influences these two components in a very different manner. This procedure has been previously employed by several authors in a variety of semi-metals [5, 24–26].

Figure 2a shows the field dependence of thermal conductivity at different temperatures. One can see that at low temperature, thermal conductivity decreases rapidly with magnetic field and then becomes flat. The electronic thermal conductivity is rapidly suppressed under the magnetic field (reflecting the very large electrical magnetoresistance of the system). In contrast to this, the phonon thermal conductivity remains almost unaffected. At 10 K, a 3 T magnetic field is high enough to suppress the amplitude of the electronic thermal conductivity by many orders of magnitude. Therefore, we can obtain electron thermal conductivity (κ_e) by subtracting the thermal conductivity at 3 T (which is equivalent to κ_{ph}) from the total thermal conductivity at zero-magnetic-field ($\kappa_{total}(B=0)$).

As the temperature rises, the electron (and hole) mobility decreases, the thermal magnetoresistance of electrons becomes less drastic and the separation of the phononic and electronic components become less straightforward. In this temperature range the field dependence of thermal conductivity can be fitted by this empirical expression [9]:

$$\kappa_{total} = \kappa_{ph} + \frac{T}{\alpha + \beta B^\gamma} \quad (1)$$

The first term on the right side of the equation corresponds to the *field-independent* phononic component, κ_{ph} . The second term corresponds to the *field-dependent* electronic component. The functional form of this second term mimics the field dependence of a magnetoresistance with a power law field dependence. Among the three fitting parameters, only α and β vary with temperature. $\gamma \approx 1.45$ remains constant in our range of investigation. Figure 2b shows κ_e and κ_{ph} extracted for sample S3 with this procedure. κ_{ph} is larger than κ_e above 3 K and dominates the thermal conductivity, consistent with the ratio L/L_0 exceeding unity with warming (Figure 1d).

Having separated the two components of thermal conductivity, let us now consider the electronic Lorenz number: $L_e = \kappa_e \rho / T$. The evolution of L_e/L_0 with temperature in different samples are presented in Figure 2c, at temperatures below 2 K and above 100 K, $L_e/L_0 \approx 1$, that is the WF law is recovered. However, around 20 K, $L_e/L_0 \ll 1$. Comparing the three samples, one sees that, in the cleanest sample (S3) L_e/L_0 shows the strongest deviation from unity.

The finite temperature downward deviation from the WF law is traditionally attributed to the presence of inelastic small-angle scattering. In presence of inelastic scattering, thermal and electrical transport are affected in different ways, referred to as “horizontal” and “vertical” processes [8, 27]. The thermal resistivity is

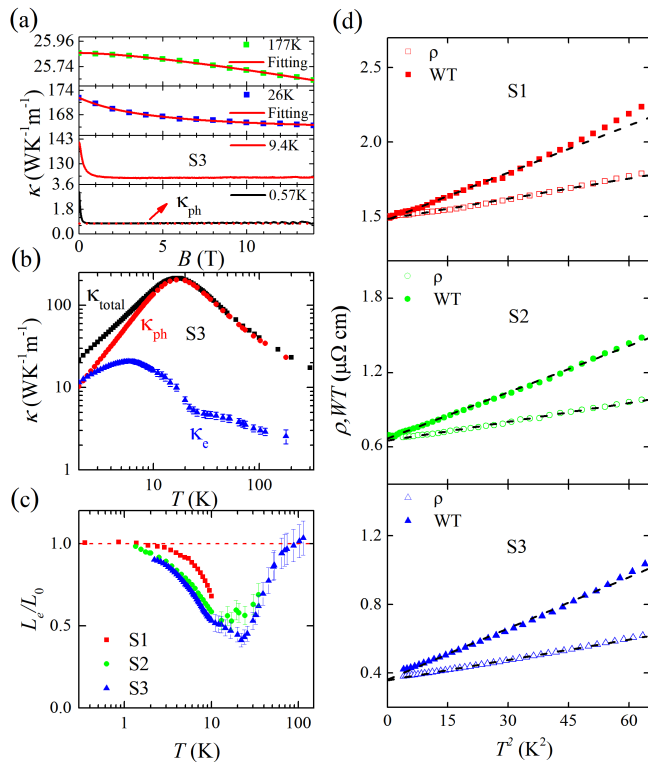


FIG. 2. **The departure from the WF law and the T^2 resistivities.** (a) Magnetic field dependence of the thermal conductivity of sample S3 at several different temperatures. The solid lines in red show the fitting of formula (1), and the electron and phonon thermal conductivity can be separated by the fitting. The dashed line represents that the phonon thermal conductivity does not change with the magnetic field after the electron thermal conductivity is suppressed. (b) The temperature dependence of electronic, phononic and total thermal conductivity of sample S3. Error bars are due to the fitting errors. (c) The temperature dependence of L_e/L_0 , $L_e = \kappa_e \rho / T$ is the electronic Lorenz number, L_0 is the Sommerfeld constant. (d) Thermal and electrical resistivities plotted as functions of T^2 , the solid symbols represent thermal resistivity and the hollow symbols represent electrical resistivity. The black dashed line is a linear fitting to the data, and the slopes of the fitting to the solid and hollow symbols are the T-square prefactors of the thermal and electrical resistivities, respectively.

affected by the two processes while the electrical resistivity is only affected by the horizontal process. As a consequence, L_e/L_0 will be degraded with warming. In the hydrodynamic picture, momentum-conserving collisions are also considered. In this case, momentum-conserving electron-electron collisions, which do not affect the electric current flow would still influence the heat flow, pulling down the L_e/L_0 ratio.

As in the case of Sb [5], a way to distinguish between these two scenarios, is to study samples with different levels of purity. In the hydrodynamic picture, the deviation from the WF law becomes more pronounced with the relative abundance of momentum-conserving elec-

tron-electron collisions compared to electron-boundary or electron-defect collisions. On the other hand, the relative weight of e-e small-angle scattering, which depends on Fermi surface geometry and the screening length [28] is not expected to change with residual resistivity. Therefore, our observation that the attenuation of L/L_0 amplifies with sample purity is in agreement with the expectations of the hydrodynamic picture [15] and in agreement with the detection of a Poiseuille flow of electrons in this system [29].

Inelastic e-e scattering can degrade the momentum flow by two known mechanisms [30, 31]. The first is through Umklapp collisions, which are rare in WTe_2 . Umklapp events cannot occur when $4k_F^{max} < G$, the width of the Brillouin zone is $G = 2\pi/c = 4.5 \text{ nm}^{-1}$ ($c = 1.4 \text{ nm}$ is the lattice parameter). Considering the mild anisotropy of the Fermi surface [2], we get $4k_a = 2.2 \text{ nm}^{-1}$, $4k_b = 2.9 \text{ nm}^{-1}$, $4k_c = 5.0 \text{ nm}^{-1}$. Only the latter is slightly larger than G . Therefore, Umklapp collisions are possible but rare. The second mechanism, proposed by Baber [32] requires multiple Fermi surfaces and can operate in WTe_2 .

Figure 2d shows the temperature dependence of electrical resistivity, ρ and thermal resistivity, $WT = (\frac{\kappa}{L_0 T})^{-1}$, for the three samples. The horizontal axis is the square of temperature. One can see that in all cases, ρ follows $\rho = \rho_0 + AT^2$ and WT follows $WT = (WT)_0 + BT^2$, ρ_0 and WT_0 are the residual resistivity associated with impurities. Their amplitude is locked to each other by the WF law. A and B are the prefactor of the T^2 resistivity. As seen in the figure, while the intercepts are identical, the slopes are different implying that $B > A$. Similar behavior has been observed in many metals [21], such as W [19], Sb [5], WP_2 [8], UPt_3 [33], CeRhIn_5 [27] and $\text{SrTi}_{1-x}\text{Nb}_x\text{O}_3$ [22]. In all these cases, $B > A$, compatible with both scenarios of the Lorenz number. However, to the best of our knowledge, only in antimony and in the present study, an evolution of B/A ratio with the variation of residual resistivity has been sought and found. As discussed in the supplement, this variation is weaker in WTe_2 than in Sb.

Let us now consider the phonon thermal conductivity κ_{ph} . As seen in figure 2b, it dominates thermal conductivity in almost all our range of investigation. Figure 3a shows the temperature dependence of the extracted phonon mean-free-path using $\ell_{ph} = \frac{3\kappa_{ph}}{\langle v_s \rangle C_{ph}}$ (See supplement for details). ℓ_{ph} increases with decreasing temperature, It tends to become comparable to the sample size well below 0.3 K, which is our lowest temperature of investigation. What impedes phonon to become ballistic at $T \approx 4 \text{ K}$? Phonon-phonon scattering, can decay heat current only if collisions are Umklapp. At 4 K, the typical wave-vector of an acoustic phonon ($\frac{k_B T}{\hbar v_s}$) is too short compared to width of the Brillouin zone to allow Umklapp scattering. The wavelength of phonons is also too long to allow scattering by point defects. In crystalline insulators phonons become ballistic in this temperature [13, 34]. Phonons are either scattered by extended disor-

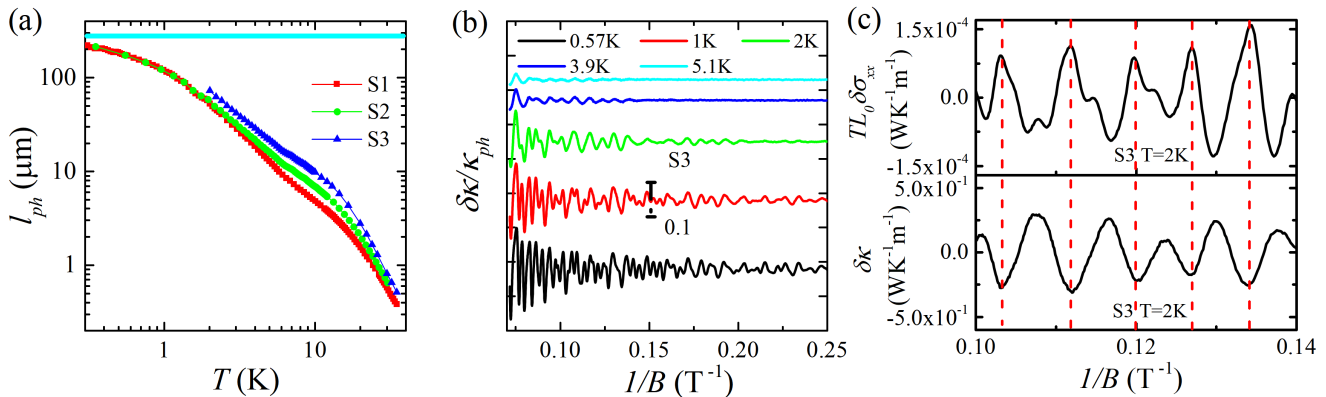


FIG. 3. **The phonon mean-free-path and quantum oscillations.** (a) The phononic mean-free-path as a function of temperature. The mean-free-path is much shorter than the effective thickness of the samples shown by the light blue horizontal line. This implies that phonons are not ballistic, but scattered by electrons. (b) The normalized amplitude of the oscillatory thermal conductivity, $\delta\kappa/\kappa_{ph}$ as a function of $1/B$ for various temperatures. Data for different temperature are shifted for clarity. The scale bar corresponds to a relative amplitude of 10%. (c) Quantum oscillations of thermal conductivity compared to oscillations of electrical conductivity in comparable units, $TL_0\delta\sigma_{xx}$. Red dashed lines correspond to the maximum and minimum of the two set of oscillations, which are out of phase.

der or by mobile electrons.

Examination of the quantum oscillations of electrical and thermal transport in WTe_2 provides a clue. The oscillatory part of the thermal conductivity, obtained after subtracting a smooth background, is shown in Figure 3b. (See the supplement for the Fourier transform and the discussion of main frequencies). Figure 3c compares this oscillatory part of the thermal conductivity, $\delta\kappa$ with Shubnikov-de Haas oscillations of the electrical conductivity normalized with the WF law. One can see that the amplitude of oscillations in $\delta\kappa$ is 3 orders of magnitude larger than in $TL_0\delta\sigma_{xx}$ (the *order of magnitude* of the electronic component). The maximum and minimum of the $TL_0\delta\sigma_{xx}$ and $\delta\kappa$ are out of phase. Similar features were reported in TaAs [35], NbP [36], TaAs₂ and NbAs₂ [37], where $\delta\kappa$ was found to be 2 orders of magnitude larger than $TL_0\delta\sigma_{xx}$. In Sb [9], a 5 orders of magnitude discrepancy was found. In the latter case, the oscillations were attributed to phonons and their strong coupling with electrons. This is backed by the fact that oscillations are out of phase. Each time electrical conductivity has a peak due to a peak in the density of states caused by the evacuation of a Landau level, the phonon thermal conductivity shows a minimum. The case of WTe_2 is similar. Mobile electrons are therefore the main reason for the short mean-free-path of phonons at cryogenic temperatures, seen in figure 3a (See the supplement for a discussion of the Dingle mobility and its orders of magnitude discrepancy with transport mobility).

Figure 4a compares the phonon mean-free-path in WTe_2 and in Sb (See the supplement for details on how to obtain the phonon mean-free-path and phonon specific heat). Despite the comparable order of magnitude, there is a qualitative difference. In Sb [9], the temperature dependence of the mean-free-path is non-monotonous as observed in Bi [34], in black P [13] and in graphite [14].

In all this cases, this was attributed to strong normal (that is non-Umklapp) scattering among phonons. In a limited temperature window, they lead to an increase in the mean-free-path with warming. This feature is absent in WTe_2 . Interestingly, as seen in figure 4b, the temperature dependence of the specific heat is remarkably different in the two systems. In WTe_2 , the Debye approximation holds below 5 K where $C_{ph} \propto T^3$ and a downward deviation starts afterwards. In Sb, the specific heat has a non-trivial temperature dependence indicating strong anharmonicity. Interestingly, the temperature dependence of specific heat in bismuth is also non-trivial [38]. This correlation between two distinct experimental features confirms that anharmonicity (i.e. a non-quadratic phonon density of states) amplifies normal ph-ph collisions, indispensable for phonon hydrodynamics.

Scrutinizing the temperature dependence of resistivity reveals another important feature of the interplay between phonons and electrons. In the Bloch-Grüneisen picture of resistivity driven by electron-phonon scattering, the electrical resistivity is linear at high temperature (when the electron-phonon scattering is quasi-elastic) and becomes $\propto T^5$ at low temperatures when the population of acoustic phonons and their typical wave-vector rapidly shrinks. The exponent of electric resistivity (following $\rho = \rho_0 + T^\gamma$) can be extracted using $\gamma = \frac{\partial \ln(\rho - \rho_0)}{\partial \ln T}$ [9, 39]. Figure 4b compares γ in WTe_2 and in Sb. One can see that in both cases, the Bloch-Grüneisen picture suddenly breaks down below 10 K. Resistivity becomes purely $\propto T^2$. This becomes understandable by taking into account the fact that ph-ph collisions are no more Umklapp below 10 K. Therefore, a momentum taken by the phonon reservoir through an e-ph collision will eventually return back to the electron reservoir through an-

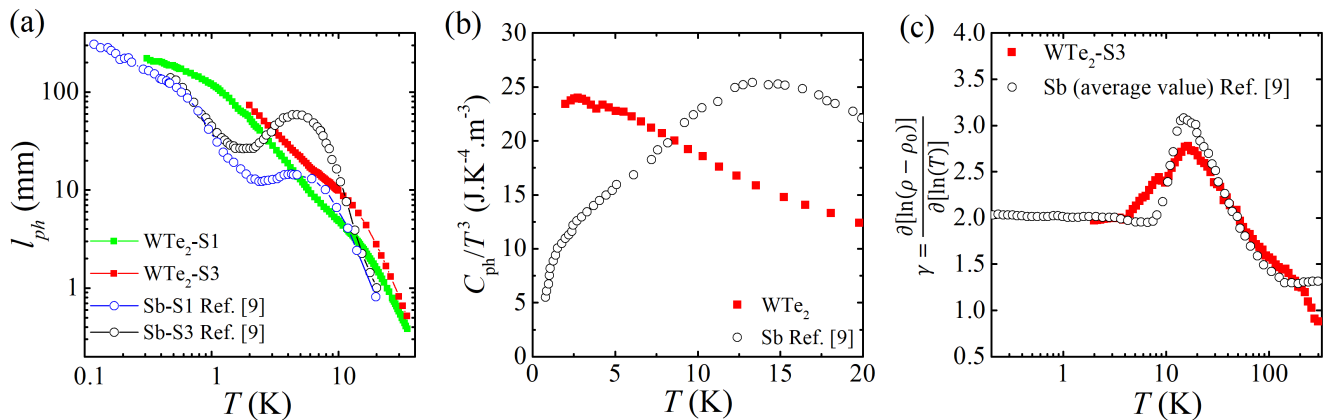


FIG. 4. **Comparison with antimony.** (a) The temperature dependence of phonon mean-free-path, l_{ph} in WTe₂ and in Sb [9]. In both cases, the phonon mean-free-path remains much smaller than the sample size due to scattering by electrons. In antimony, l_{ph} is non-monotonous, but in WTe₂, it shows only a mild shoulder. This indicates that normal ph-ph scattering in WTe₂ is weak and there is no clear regime of phonon hydrodynamics. (b) Phonon specific heat divided by the cube of temperature in the two semimetals. It is flat below 5 K and smoothly decreases with warming, indicating that phonon density of states (PDOS) is quadratic and anharmonicity is weak, in contrast to Sb [9], where PDOS has a non-trivial frequency dependence. (c) The amplitude of the exponent of the electric resistivity ($\rho = \rho_0 + T^\gamma$) in WTe₂ and in Sb [9]. In both cases, the smooth increase of γ with cooling is suddenly disrupted at a temperature below which Umklapp ph-ph scattering becomes impossible. In both cases, below ≈ 10 K, only e-e (and not e-ph) collisions contribute to decay of momentum flow.

other ph-e collision. As a consequence, e-ph collisions do not degrade the momentum flow of electrons. Note that in contrast to Sb, in WTe₂, the phonon scattering time is much longer than the e-e scattering time (see the supplement).

In summary, we studied the electrical and thermal transport properties of WTe₂ at low temperatures, and found that the finite temperature deviation from the WF law is amplified with sample quality as expected in the hydrodynamic picture of electron transport. Phonons are strongly scattered by electrons, but there is no signature of purely phononic hydrodynamics, presumably due to the weakness of normal ph-ph collisions. At cryogenic temperatures, there is substantial momentum exchange between the electronic and phononic reservoirs. Phonons cannot loose momentum alone, but electrons can, and

this leads to the disruption of the Bloch-Grüneisen picture and the emergence of a purely T^2 resistivity.

This work was supported by The National Key Research and Development Program of China (Grant No.2022YFA1403500), the National Science Foundation of China (Grant No. 12004123, 51861135104 and 11574097), and the Fundamental Research Funds for the Central Universities (Grant no. 2019kfyXMBZ071). K. B. was supported by the Agence Nationale de la Recherche (ANR-19-CE30-0014-04). X. L. acknowledges the China National Postdoctoral Program for Innovative Talents (Grant No.BX20200143) and the China Postdoctoral Science Foundation (Grant No.2020M682386).

*zengwei.zhu@hust.edu.cn

*kamran.behnia@espci.fr

-
- [1] M. N. Ali, J. Xiong, S. Flynn, J. Tao, Q. D. Gibson, L. M. Schoop, T. Liang, N. Haldolaarachchige, M. Hirschberger, N. P. Ong, and R. J. Cava, Large, non-saturating magnetoresistance in WTe₂, *Nature* **514**, 205 (2014).
- [2] Z. Zhu, X. Lin, J. Liu, B. Fauqué, Q. Tao, C. Yang, Y. Shi, and K. Behnia, Quantum oscillations, thermoelectric coefficients, and the fermi surface of semimetallic WTe₂, *Phys. Rev. Lett.* **114**, 176601 (2015).
- [3] Y. Wang, L. Wang, X. Liu, H. Wu, P. Wang, D. Yan, B. Cheng, Y. Shi, K. Watanabe, T. Taniguchi, S. Liang, and F. Miao, Direct evidence for charge compensation-induced large magnetoresistance in thin WTe₂, *Nano Letters* **19**, 3969 (2019).
- [4] A. A. Soluyanov, D. Gresch, Z. Wang, Q. Wu, M. Troyer, X. Dai, and B. A. Bernevig, Type-II Weyl semimetals, *Nature* **527**, 495 (2015).
- [5] A. Jaoui, B. Fauqué, and K. Behnia, Thermal resistivity and hydrodynamics of the degenerate electron fluid in antimony, *Nature Communications* **12**, 195 (2021).
- [6] B. Fauqué, X. Yang, W. Tabis, M. Shen, Z. Zhu, C. Proust, Y. Fuseya, and K. Behnia, Magnetoresistance of semimetals: The case of antimony, *Phys. Rev. Mater.* **2**, 114201 (2018).
- [7] J. Gooth, F. Menges, N. Kumar, V. Süß, C. Shekhar, Y. Sun, U. Drechsler, R. Zierold, C. Felser, and B. Gotsmann, Thermal and electrical signatures of a hydrodynamic electron fluid in tungsten diphosphide, *Nature Communications* **9**, 4093 (2018).
- [8] A. Jaoui, B. Fauqué, C. W. Rischau, A. Subedi, C. Fu,

- J. Gooth, N. Kumar, V. Süß, D. L. Maslov, C. Felser, and K. Behnia, Departure from the Wiedemann–Franz law in WP_2 driven by mismatch in T -square resistivity prefactors, *npj Quantum Materials* **3**, 64 (2018).
- [9] A. Jaoui, A. Gourgout, G. Seyfarth, A. Subedi, T. Lorenz, B. Fauqué, and K. Behnia, Formation of an electron-phonon bifluid in bulk antimony, *Phys. Rev. X* **12**, 031023 (2022).
- [10] R. N. Gurzhi, Hydrodynamic effects in solids at low temperature, *Soviet Physics Uspekhi* **11**, 255 (1968).
- [11] C. Jesse, K. S. Jing, W. Ke, L. Xiaomeng, H. Achim, L. Andrew, S. Subir, K. Philip, T. Takashi, W. Kenji, A. O. Thomas, and F. Kin Chung, Observation of the Dirac fluid and the breakdown of the Wiedemann-Franz law in graphene, *Science* **351**, 1058 (2016).
- [12] V. Martelli, J. L. Jiménez, M. Continentino, E. Baggio-Saitovitch, and K. Behnia, Thermal transport and phonon hydrodynamics in strontium titanate, *Phys. Rev. Lett.* **120**, 125901 (2018).
- [13] M. Yo, S. Alaska, A. Kazuto, M. Atsushi, T. Masashi, A. Yuichi, I. Koichi, and B. Kamran, Observation of Poiseuille flow of phonons in black phosphorus, *Science Advances* **4**, eaat3374 (2018).
- [14] M. Yo, M. Nayuta, I. Takayuki, and B. Kamran, Phonon hydrodynamics and ultrahigh-room-temperature thermal conductivity in thin graphite, *Science* **367**, 309 (2020).
- [15] A. Principi and G. Vignale, Violation of the Wiedemann-Franz law in hydrodynamic electron liquids, *Phys. Rev. Lett.* **115**, 056603 (2015).
- [16] J. Coulter, G. B. Osterhoudt, C. A. C. Garcia, Y. Wang, V. M. Plisson, B. Shen, N. Ni, K. S. Burch, and P. Narang, Uncovering electron-phonon scattering and phonon dynamics in type-I Weyl semimetals, *Phys. Rev. B* **100**, 220301 (2019).
- [17] A. Levchenko and J. Schmalian, Transport properties of strongly coupled electron-phonon liquids, *Annals of Physics* **419**, 168218 (2020).
- [18] X. Huang and A. Lucas, Electron-phonon hydrodynamics, *Phys. Rev. B* **103**, 155128 (2021).
- [19] D. K. Wagner, J. C. Garland, and R. Bowers, Low-temperature electrical and thermal resistivities of tungsten, *Phys. Rev. B* **3**, 3141 (1971).
- [20] J. Paglione, M. A. Tanatar, D. G. Hawthorn, R. W. Hill, F. Ronning, M. Sutherland, L. Taillefer, C. Petrovic, and P. C. Canfield, Heat transport as a probe of electron scattering by spin fluctuations: The case of antiferromagnetic $CeRhIn_5$, *Phys. Rev. Lett.* **94**, 216602 (2005).
- [21] K. Behnia, On the origin and the amplitude of T -square resistivity in fermi liquids, *Annalen der Physik* **534**, 2100588 (2022).
- [22] S. Jiang, B. Fauqué, and K. Behnia, T -square dependence of the electronic thermal resistivity of metallic strontium titanate, *Phys. Rev. Lett.* **131**, 016301 (2023).
- [23] J. Heremans, J. P. Issi, A. A. M. Rashid, and G. A. Saunders, Electrical and thermal transport properties of arsenic, *Journal of Physics C: Solid State Physics* **10**, 4511 (1977).
- [24] G. K. White and S. B. Woods, The thermal and electrical resistivity of bismuth and antimony at low temperatures, *The Philosophical Magazine: A Journal of Theoretical Experimental and Applied Physics* **3**, 342 (1958).
- [25] C. Uher and H. J. Goldsmid, Separation of the electronic and lattice thermal conductivities in bismuth crystals, *physica status solidi (b)* **65**, 765 (1974).
- [26] F. Han, N. Andrejevic, T. Nguyen, V. Kozii, Q. T. Nguyen, T. Hogan, Z. Ding, R. Pablo-Pedro, S. Parjan, B. Skinner, A. Alatas, E. Alp, S. Chi, J. Fernandez-Baca, S. Huang, L. Fu, and M. Li, Quantized thermoelectric Hall effect induces giant power factor in a topological semimetal, *Nature Communications* **11**, 6167 (2020).
- [27] J. Paglione, M. A. Tanatar, D. G. Hawthorn, R. W. Hill, F. Ronning, M. Sutherland, L. Taillefer, C. Petrovic, and P. C. Canfield, Heat transport as a probe of electron scattering by spin fluctuations: The case of antiferromagnetic $CeRhIn_5$, *Phys. Rev. Lett.* **94**, 216602 (2005).
- [28] S. Li and D. L. Maslov, Lorentz ratio of a compensated metal, *Phys. Rev. B* **98**, 245134 (2018).
- [29] U. Vool, A. Hamo, G. Varnavides, Y. Wang, T. X. Zhou, N. Kumar, Y. Dovzhenko, Z. Qiu, C. A. C. Garcia, A. T. Pierce, J. Gooth, P. Anikeeva, C. Felser, P. Narang, and A. Yacoby, Imaging phonon-mediated hydrodynamic flow in WTe_2 , *Nature Physics* **17**, 1216 (2021).
- [30] X. Lin, B. Fauqué, and K. Behnia, Scalable T^2 resistivity in a small single-component Fermi surface, *Science* **349**, 945 (2015).
- [31] J. Wang, J. Wu, T. Wang, Z. Xu, J. Wu, W. Hu, Z. Ren, S. Liu, K. Behnia, and X. Lin, T -square resistivity without umklapp scattering in dilute metallic Bi_2O_2Se , *Nature Communications* **11**, 3846 (2020).
- [32] W. G. Baber, The contribution to the electrical resistance of metals from collisions between electrons, *Proceedings of the Royal Society of London. Series A - Mathematical and Physical Sciences* **158**, 383 (1937).
- [33] B. Lussier, B. Ellman, and L. Taillefer, Anisotropy of heat conduction in the heavy fermion superconductor UPt_3 , *Phys. Rev. Lett.* **73**, 3294 (1994).
- [34] V. Kopylov and L. Mezghov-Deglin, Investigation of the kinetic coefficients of bismuth at helium temperatures, *Sov. Phys. JETP* **38**, 357 (1973).
- [35] J. Xiang, S. Hu, Z. Song, M. Lv, J. Zhang, L. Zhao, W. Li, Z. Chen, S. Zhang, J.-T. Wang, Y.-f. Yang, X. Dai, F. Steglich, G. Chen, and P. Sun, Giant magnetic quantum oscillations in the thermal conductivity of TaAs: Indications of chiral zero sound, *Phys. Rev. X* **9**, 031036 (2019).
- [36] P. K. Tanwar, M. S. Alam, M. Ahmad, D. Kaczorowski, and M. Matusiak, Severe violation of the Wiedemann-Franz law in quantum oscillations of NbP, *Phys. Rev. B* **106**, L041106 (2022).
- [37] X. Rao, X. Zhao, X.-Y. Wang, H. Che, L. G. Chu, G. Hussain, T. Xia, and X. F. Sun, Quantum oscillation of thermal conductivity and violation of Weidemann-Franz law in TaAs₂ and NbAs₂, *arXiv: Materials Science* (2019).
- [38] L. E. Díaz-Sánchez, A. H. Romero, M. Cardona, R. K. Kremer, and X. Gonze, Effect of the spin-orbit interaction on the thermodynamic properties of crystals: Specific heat of bismuth, *Phys. Rev. Lett.* **99**, 165504 (2007).
- [39] R. A. Cooper, Y. Wang, B. Vignolle, O. J. Lipscombe, S. M. Hayden, Y. Tanabe, T. Adachi, Y. Koike, M. Nohara, H. Takagi, C. Proust, and N. E. Hussey, Anomalous criticality in the electrical resistivity of $La_{2-x}Sr_xCuO_4$, *Science* **323**, 603 (2009).

Supplemental Material for
Purity-dependent Lorenz number, electron hydrodynamics and electron-phonon coupling in WTe₂

Wei Xie¹, Feng Yang¹, Liangcai Xu¹, Xiaokang Li¹, Zengwei Zhu^{1,*} and Kamran Behnia^{2,*}

¹ *Wuhan National High Magnetic Field Center and School of Physics, Huazhong University of Science and Technology, Wuhan, 430074, China*

² *Laboratoire de Physique et Etude des Matériaux (CNRS/UPMC), Ecole Supérieure de Physique et de Chimie Industrielles, 10 Rue Vauquelin, 75005 Paris, France*

S1. Samples and Methods.

High quality single crystals of WTe₂ were grown by Te-flux method. W(99.95%) and excessive amounts of Te(99.999%) powder were sealed in alumina ampoule, and then sealed in quartz tube. The quartz tube was heated up to 1050°C over 12 h and kept for 12 h, then cooled down slowly to 700°C. We obtained WTe₂ single crystals with different qualities by changing cooling rate. Shining crystals were mechanically separated from the flux with care.

The transport measurements were performed with home-built one-heater-two-thermometers or one-heater-two-thermocouples setups, which allowed us to measure the electrical resistivity and the thermal conductivity with the same electrodes. Above 2 K, We performed them in a physical property measurement system (Quantum Design) and between 300 mK to 10 K, in a Leiden dilution refrigerator (CF-CS81-1700-Maglev). Between 300 mK and 4 K, CX-1010 Cernox chips and RuO₂ thermometers were used to measure the temperature, while the CX-1030 Cernox chips were used between 300 mK and 40 K. And the type E thermocouples were used between 20 K and room temperature. The thermal gradient in the sample was produced through a 10 kΩ chip resistor. The electrical transport measurements were measured by A standard four-probe method.

S2. Magnetoresistance and the electronic thermal conductivity

The large magnetoresistance of WTe₂ triggered the interest in this material [14]. We observed a magnetoresistance as large as 10⁵%-10⁶% at 2 K, when the applied field of 14 T, as shown in Figure S1a. Magnetoresistance rapidly increases to 10⁴%-10⁵% with a field of 3 T. We can separate phononic thermal conductivity by suppressing electronic thermal conductivity with a moderate magnetic field. Figure S1b shows the electronic thermal conductivity plotted as κ_e/T , separated in this way. Dashed lines represent L_0/ρ_0 for different samples. The good agreement between them and κ_e/T at low temperature corresponds to verification of WF law and verifies the accuracy of applying a magnetic field to separate the electronic and phononic thermal conductivity.

S3. Specific heat and phononic mean free path.

Figure S2 shows the temperature dependence of specific heat. A $C/T = \gamma + \beta T^2$ fit to the low temperature data is shown in the inset. The intercept corresponds to the electronic specific heat $\gamma=1.92$ mJ·mol⁻¹·K⁻² and the slope corresponds to the phononic specific heat $\beta=1.09$ mJ·mol⁻¹·K⁻². The phononic specific heat below 2 K is obtained by extrapolating the phononic specific heat measured at low temperature. This is reasonable, given the T^3 temperature dependence of phononic specific heat below 5 K. The phononic mean free path can be extracted using the relation $\ell_{ph} = \frac{3\kappa_{ph}}{C_{ph}\langle v_s \rangle}$, with $\langle v_s \rangle=2200$ m·s⁻¹[15]. For different samples, ℓ_{ph} is shown in the main text.

S4. FFT analysis of the quantum oscillations.

Figure S3a shows the results of the FFT of the oscillatory part of the magnetoresistance. Four main frequencies are observed. The four frequencies are 93 T, 126 T, 144 T and 163 T, very close to the values reported before, and attributed to the two electron pockets and the two hole pockets [16]. Quantum oscillation of thermal conductivity can be analyzed in the similar way to that of magnetoresistance. After subtracting a smooth background of the thermal conductivity, the oscillatory part is obtained. The FFT of the oscillatory part of the thermal conductivity is presented in Figure S3b. Four main frequencies consistent with those found in electrical conductivity are detected and shown in Figure S3a.

S5. Dingle analysis.

Using $\mu_{tr} = 1/(n+p)e\rho_0$, we can get the transport mobility $\mu_{tr}=63$ T⁻¹ of sample S3. As shown in Figure S4, the Dingle analysis gives the Dingle mobility $\mu_D=0.2$ T⁻¹ of the same sample. The dashed line in Figure S4b are almost parallel, indicating that the three samples have similar Dingle mobility, although the residual resistivity and the transport mobility of sample S1 and S3 is four times different, and the Dingle mobility of sample S3 is only about 1.1 times larger than that of sample S1, see the table S2. And μ_{tr} is more than 2 orders of magnitude

larger than μ_D , and the similar phenomenon has been reported in some semimetals before, such as Cd_3As_2 , WP_2 and Sb , Table S3 shows the two mobilities and the ratio of various semimetals.

As we can see in Figure S4c, the electronic scattering time (τ_e) extracted from the electrical resistivity is more than 2 orders of magnitude larger than the Dingle scattering time (τ_D) extracted from the Dingle analysis in our cleanest sample S3, while in Cd_3As_2 [2], WP_2 [3] and Sb [13] with larger RRR, τ_e is 3-4 orders of magnitude

larger than τ_D .

S6. κ_e and κ_{ph} in the two materials.

Figure S5a shows κ_e as a function of temperature in WTe_2 and Sb [13]. One can see that κ_e in WTe_2 is one order of magnitude smaller than that in Sb . Figure S5b shows the temperature dependence of κ_{ph} in the two materials. Above its maximum, κ_{ph} is similar in the two systems. Below its peak, it decreases more rapidly in Sb , consistent with a stronger e-ph coupling in the latter compared to WTe_2 .

-
- [1] A. Jaoui, B. Fauqué, and K. Behnia, Thermal resistivity and hydrodynamics of the degenerate electron fluid in antimony, *Nature Communications* **12**, 195 (2021).
- [2] T. Liang, Q. Gibson, M. N. Ali, M. Liu, R. J. Cava, and N. P. Ong, Ultrahigh mobility and giant magnetoresistance in the Dirac semimetal Cd_3As_2 , *Nature Materials* **14**, 280 (2015).
- [3] N. Kumar, Y. Sun, N. Xu, K. Manna, M. Yao, V. Süss, I. Leermakers, O. Young, T. Förster, M. Schmidt, H. Borrmann, B. Yan, U. Zeitler, M. Shi, C. Felser, and C. Shekhar, Extremely high magnetoresistance and conductivity in the type-II Weyl semimetals WP_2 and MoP_2 , *Nature Communications* **8**, 1642 (2017).
- [4] Y. Luo, N. J. Ghimire, M. Wartenbe, H. Choi, M. Neupane, R. D. McDonald, E. D. Bauer, J. Zhu, J. D. Thompson, and F. Ronning, Electron-hole compensation effect between topologically trivial electrons and nontrivial holes in NbAs , *Phys. Rev. B* **92**, 205134 (2015).
- [5] K. Yokoi, H. Murakawa, M. Komada, T. Kida, M. Hagiwara, H. Sakai, and N. Hanasaki, Enhanced magnetoresistance in the binary semimetal NbAs_2 due to improved crystal quality, *Phys. Rev. Mater.* **2**, 024203 (2018).
- [6] W. Gao, N. Hao, F.-W. Zheng, W. Ning, M. Wu, X. Zhu, G. Zheng, J. Zhang, J. Lu, H. Zhang, C. Xi, J. Yang, H. Du, P. Zhang, Y. Zhang, and M. Tian, Extremely Large Magnetoresistance in a Topological Semimetal Candidate Pyrite PtBi_2 , *Phys. Rev. Lett.* **118**, 256601 (2017).
- [7] F. F. Tafti, Q. Gibson, S. Kushwaha, J. W. Krizan, N. Haldolaarachchige, and R. J. Cava, Temperature-field phase diagram of extreme magnetoresistance, *Proceedings of the National Academy of Sciences* **113**, E3475 (2016).
- [8] C.-L. Zhang, Z. Yuan, Q.-D. Jiang, B. Tong, C. Zhang, X. C. Xie, and S. Jia, Electron scattering in tantalum monoarsenide, *Phys. Rev. B* **95**, 085202 (2017).
- [9] C. Shekhar, A. K. Nayak, Y. Sun, M. Schmidt, M. Nicklas, I. Leermakers, U. Zeitler, Y. Skourski, J. Wosnitza, Z. Liu, Y. Chen, W. Schnelle, H. Borrmann, Y. Grin, C. Felser, and B. Yan, Extremely large magnetoresistance and ultrahigh mobility in the topological Weyl semimetal candidate NbP , *Nature Physics* **11**, 645 (2015).
- [10] L. Zhao, J. He, D. Chen, S. Zhang, Z. Ren, and G. Chen, Extremely large magnetoresistance and Shubnikov-de Haas oscillations in the compensated semimetal W_2As_3 , *Phys. Rev. B* **99**, 205116 (2019).
- [11] L. Wu, S. Chi, H. Zuo, G. Xu, L. Zhao, Y. Luo, and Z. Zhu, Field-induced lifshitz transition in the magnetic weyl semimetal candidate pralsi, *npj Quantum Materials* **8**, 4 (2023).
- [12] F. Arnold, C. Shekhar, S.-C. Wu, Y. Sun, R. D. dos Reis, N. Kumar, M. Naumann, M. O. Ajeesh, M. Schmidt, A. G. Grushin, J. H. Bardarson, M. Baenitz, D. Sokolov, H. Borrmann, M. Nicklas, C. Felser, E. Hassinger, and B. Yan, Negative magnetoresistance without well-defined chirality in the Weyl semimetal TaP , *Nature Communications* **7**, 11615 (2016).
- [13] A. Jaoui, A. Gourgout, G. Seyfarth, A. Subedi, T. Lorenz, B. Fauqué, and K. Behnia, Formation of an electron-phonon bifluid in bulk antimony, *Phys. Rev. X* **12**, 031023 (2022).
- [14] M. N. Ali, J. Xiong, S. Flynn, J. Tao, Q. D. Gibson, L. M. Schoop, T. Liang, N. Haldolaarachchige, M. Hirschberger, N. P. Ong, and R. J. Cava, Large, non-saturating magnetoresistance in WTe_2 , *Nature* **514**, 205 (2014).
- [15] B. M. S. Ishtiaque, and S. H. Naqib, Elastic, electronic, bonding, and optical properties of WTe_2 Weyl semimetal: A comparative investigation with MoTe_2 from first principles, *Results in Physics* **19**, 103639 (2020).
- [16] Z. Zhu, X. Lin, J. Liu, B. Fauqué, Q. Tao, C. Yang, Y. Shi, and K. Behnia, Quantum oscillations, thermoelectric coefficients, and the fermi surface of semimetallic WTe_2 , *Phys. Rev. Lett.* **114**, 176601 (2015).

Sample	Size(mm ³)(width×thickness×length)	RRR	\bar{s} (mm)	l_0 (μ m)	ρ_0 ($\mu\Omega.cm$)	A($n\Omega.cm.K^{-2}$)	B($n\Omega.cm.K^{-2}$)	B/A
1	0.537×0.162×1.12	250	0.295	3.2	1.48	4.49±0.20	10.28±0.11	2.29
2	0.069×0.88×1.42	540	0.246	7.3	0.65	5.10±0.12	12.50±0.10	2.45
3	0.469×0.238×1.24	840	0.334	13.2	0.36	3.92±0.13	10.00±0.09	2.55

TABLE S1. **Details of the measured samples.** RRR is the residual resistivity ratio defined as ρ_{300K}/ρ_{2K} . $\bar{s} = \sqrt{width \times thickness}$ represents the average diameter of the conducting cross-section. The carrier mean free path l_0 was calculated from the residual resistivity ρ_0 and the expression for Drude conductivity assuming four spherical hole and four spherical electron pockets. A and B are the electrical and thermal T²-resistivities prefactors, respectively.

Sample	Carrier density (10 ¹⁹ cm ⁻³)	RRR	ρ_0 ($\mu\Omega.cm$)	μ_{tr} ($m^2V^{-1}s^{-1}$)	μ_D ($m^2V^{-1}s^{-1}$)	r	Reference
WTe ₂ S1	n=p=1.37	250	1.48	15	0.18	83	This work
WTe ₂ S2	n=p=1.37	540	0.65	35	0.18	194	This work
WTe ₂ S3	n=p=1.37	840	0.36	63	0.20	315	This work

TABLE S2. **The transport and quantum mobilities in the WTe₂ samples.** The transport mobility u_{tr} is calculated from the residual resistivity ρ_0 and carrier densities by $1/\rho_0 e(n+p)$. u_D is the Dingle mobility extracted from a Dingle analysis of the quantum oscillations. r is the ratio of μ_{tr} to μ_D . μ_D keeps almost constant while the transport mobility varies 4 times. This is similar to the case of Sb[1].

Sample	Carrier density (10 ¹⁹ cm ⁻³)	RRR	ρ_0 ($\mu\Omega.cm$)	μ_{tr} ($m^2V^{-1}s^{-1}$)	μ_D ($m^2V^{-1}s^{-1}$)	r	Reference
WTe ₂ S3	n=p=1.37	840	0.36	63	0.20	315	This work
Sb S1	n=p=5.5	260	0.159	71	0.33	215	[1]
Sb S2	n=p=5.5	430	0.0946	120	0.36	333	[1]
Sb S3	n=p=5.5	3000	0.0134	848	0.38	2231	[1]
Sb S4	n=p=5.5	1700	0.0241	772	0.38	2031	[1]
Cd ₃ As ₂	n=0.74	4100	0.021	870	0.087	10000	[2]
WP ₂	n=p=250	24850	0.005	400	0.08	5000	[3]
NbAs	n=p=1	72	—	193	0.193	1000	[4]
NbAs ₂	n=p=12	1580	0.041	62.5	~0.1	625	[5]
PtBi ₂	n=p=10	1667	0.024	6.55	0.0376	174	[6]
LaBi	n=p=20	610	0.1	15.6	0.165	95	[7]
TaAs	n=p=0.5	49	2	48	0.61	79	[8]
NbP	n=p=0.15	115	0.63	500	>10	<50	[9]
LaSb	n=p=16	170	0.6	3.3	0.125	26	[7]
W ₂ As ₃	n=p=2	1240	0.23	3	0.13	23	[10]
PrAlSi	n=p=4.75	4	15	0.5	0.33	1.5	[11]
TaP	n=p=2	8	3	3.5	3.2	1.1	[12]

TABLE S3. **The transport and quantum mobilities in different semimetals.** The transport mobility u_{tr} is calculated from the residual resistivity ρ_0 and carrier densities by $1/\rho_0 e(n+p)$. μ_D is the Dingle mobility extracted from a Dingle analysis of the quantum oscillations. r is the ratio of μ_{tr} to μ_D . Some semimetal data extracted from the references are also listed in the table for comparison.

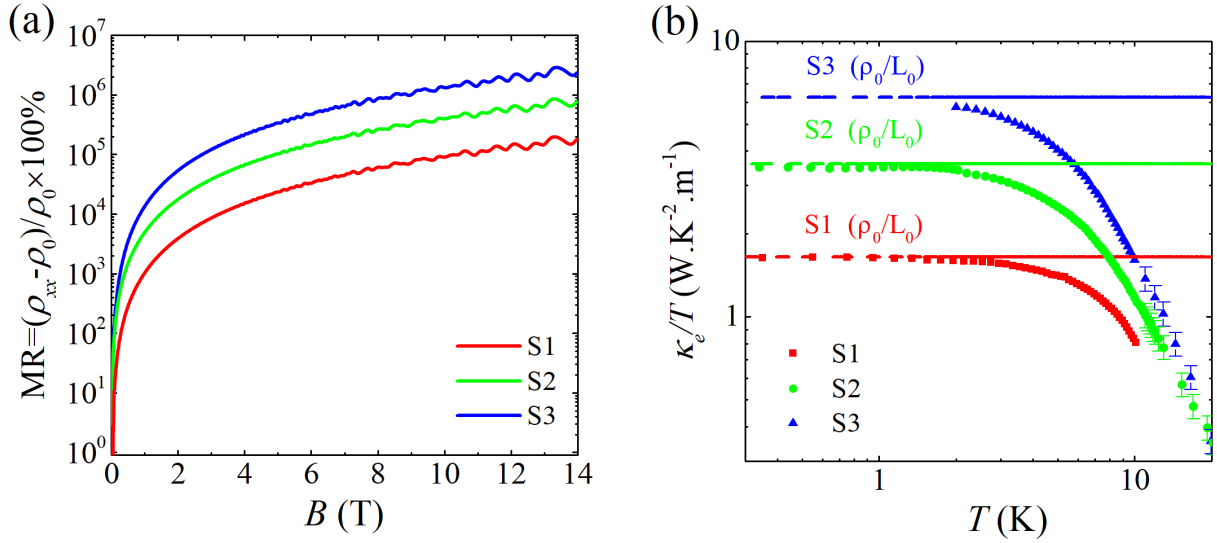


FIG. S1. **Magnetoconductance and electronic thermal conductivity of WTe₂.** (a) Magnetoconductances of different samples at $T = 2$ K. (b) Temperature dependence of the electronic thermal conductivity plotted as κ_e / T , the dashed lines represent L_0 / ρ_0 for different samples.

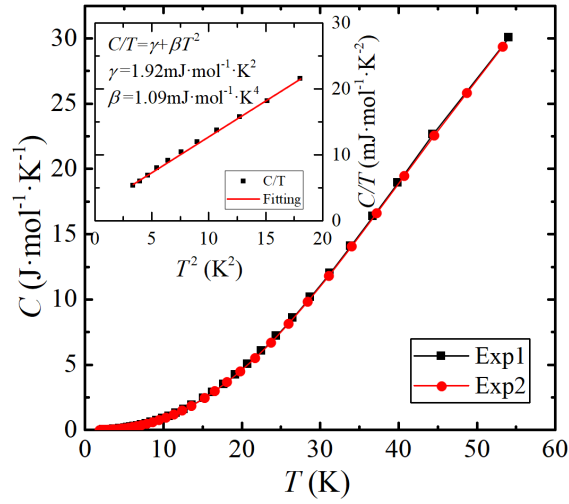


FIG. S2. **Specific heat.** Temperature dependence of the specific heat in WTe₂. The red and black points represent two measurements of different samples. Inset shows a plot of C/T vs T^2 in the low temperature range. The red line corresponds to the fitting of $C/T = \gamma + \beta T^2$.

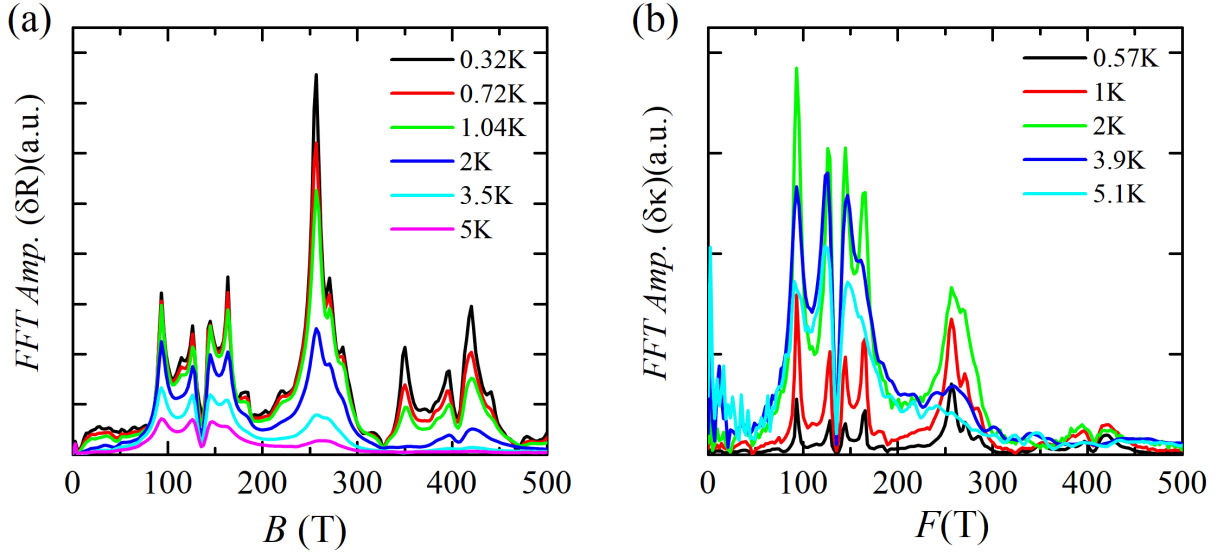


FIG. S3. **The amplitude of the fast Fourier transform of δR and $\delta \kappa$** (a) Fast Fourier transform analysis of the quantum oscillations of the magnetoresistance at several temperatures. (b) Fast Fourier transformation analysis of the quantum oscillations of the thermal conductivity at several temperatures. The four main frequencies can be observed at the quantum oscillations of magnetoresistance and thermal conductivity.

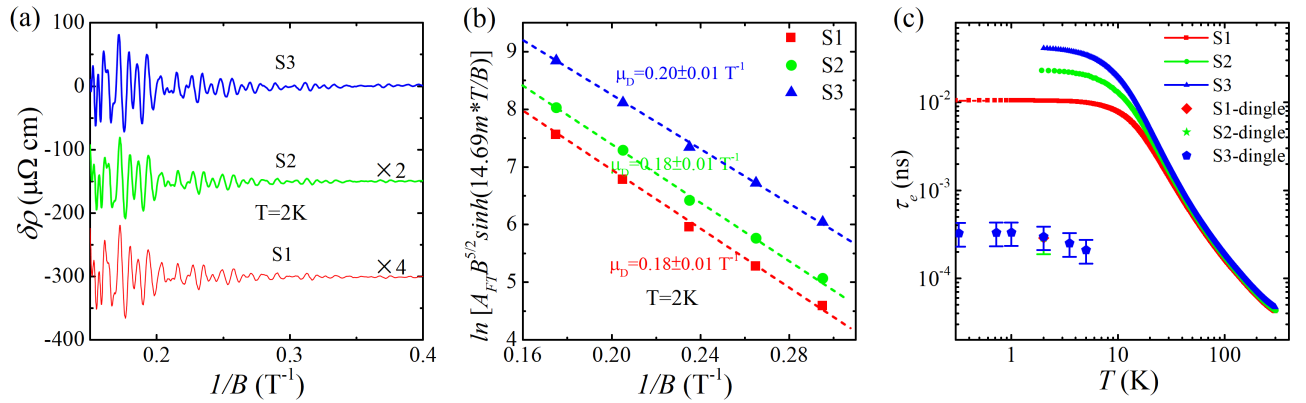


FIG. S4. **Dingle analysis of WTe_2 .** (a) Quantum oscillations of the magnetoresistance in three samples at $T=2K$. Curves are shifted vertically for clarity and multiplied by a factor 2 for S2 and 4 for S1. (b) Dingle analysis of the amplitude of the 93 T peak of the fast Fourier transform of $\delta \rho$ in different samples. The three dashed lines are almost parallel, indicating that the three samples have the same Dingle mobility. (c) Temperature dependence of the electronic scattering time extracted from the electrical resistivity and the Dingle scattering time extracted from the Dingle analysis for three WTe_2 samples

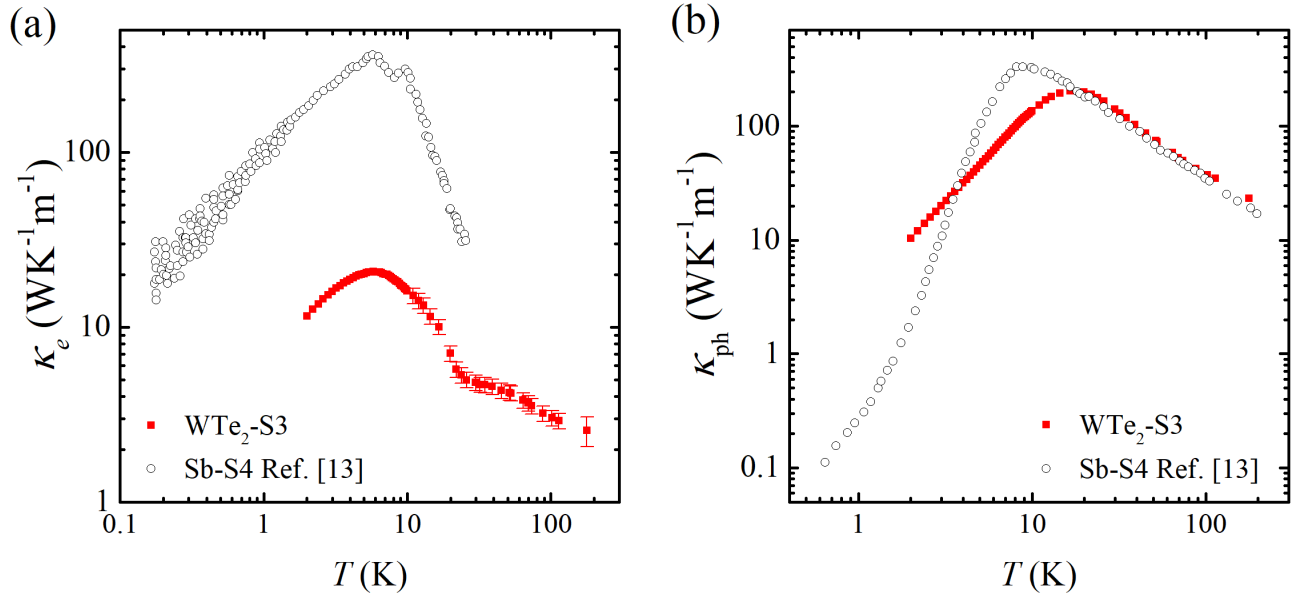


FIG. S5. Comparison of electronic and phononic thermal conductivity in WTe_2 and Sb . (a) Temperature dependence of κ_e and (b) κ_{ph} in WTe_2 and Sb [13].